INTERNATIONAL JOURNAL OF NOVEL RESEARCH AND DEVELOPMENT (IJNRD)
© 2026 IJNRD | Volume 11, Issue 5, May 2026 | ISSN: 2456-4184 | IJNRD.ORG

Photocatalytic performance of CeO_2 , SnO_2 nanoparticles catalysed by Methylene Blue (MB) dye degradation

G. Ramanathan [1], N.Srinivasan [1], K. Syed Suraj Babu[2], S. Sakthiya [3] K R Murali [4]

[1]Department of Physics, Sri Sairam Engineering College, Chennai, India

[2]Department of Physics, The New College, Royapettah, Chennai, India

[3]Department sri sairam Homoeopathy Medical College and research centre, Chennai, India

[4]Department of Theoretical physics, University of Madras, Chennai, India

Abstract:

Two different methods were used to produce powdered cerium oxide (CeO2) and tin oxide (SnO2) nanoparticles. One uses the sol gel Acrylamide procedure, and the other uses Artemisia pallens leaves (cerium (III) nitrate) in a co-precipitation process. The generated SnO2 and CeO2 powders were characterized using a variety of analytical techniques. The powder X-ray diffraction analysis revealed that the sample powder was crystalline and had a single phase cubic structure. Due to the aggregation of individual particles, the broad peaks indicate both the nanosized crystal and the increase in crystallite size with temperature. Particle size variation, lattice strain, stress, and energy density were computed using a variety of methods, including the Williamson-Hall, Monshi, and Debye's Scherer methods. The tiny crystallite size and lattice strain caused the CeO2 nanoparticles' line broadening. The Scherer formula and modified versions of W-H analysis were used to investigate this broadening. Non-uniform strains in the particles are revealed by this variation in particle size, lattice strain, stress, and energy density. As the particle size increased, so did this non-uniform strain. Through the use of transmission electron microscopy (TEM), CeO2 ultrafine nanopowder was found to include spherical particles with an average size of 4 to 16 nm. The average separation between two successive fringes in the High Resolution TEM pattern is 0.31 nm. Tin oxide and CeO2 nanoparticles that have been produced catalyze the photocatalytic destruction of MB. The pseudo first order rate constant of the MB dye was calculated for two distinct catalyst Nps based on the observation. Within 180 minutes, 19 mg/l cerium oxide caused the most degradation in the removal efficiency of MB dye using cerium, which indicates a higher efficiency (95%) compared to tin oxide catalysts (93%). The collected data show how photogenerated holes affect the dye's degradation mechanism. Using BET surface analysis techniques, cerium oxide material was examined while taking the photocatalytic activity efficiency findings into consideration. Brunauer–Emmett–Teller (BET) is a surface analysis technique that is essential for figuring out the particular surface area of a material. Surface area and pore diameters at different temperatures can be directly measured using this technique. The pore diameter ranged

from 3 to 9 nm, with an average of no more than 10 nm. As the calcination temperature increased, the average pore size increased from 3.3 to 9.1 nm.

Keywords: XRD, FESEM, TEM, UV-visible, FTIR, Photocatalyst, BET

Introduction:-

Lanthanide group, the first element with four f-type electrons, cerium, has drawn a lot of interest from researchers in the fields of physics, chemistry, biology, and material science. A cerium oxide nanoparticle can be used for a variety of medical purposes, including antioxidant, anticancer, antibacterial, and toxicological research. The rare earth element with the largest abundance, cerium, has two oxidation states [1]. Cerium oxide, also known as ceria (CeO_2), has a wide range of uses, including as catalysts and catalyst supports [2–3], oxygen ion conductors in solid oxide fuel cells [4–7], electrochemical oxygen pumps [8–10], UV absorbents [9–10], fluorescent materials [10], and amperometric oxygen ion monitors [11–12] as well as gas sensors, among other things [12–16]. Nanoceria is used extensively in high-tech, consumer, and instrument items for commercial purposes. Additionally, they function as excellent oxide ion conductors in solid oxide fuel cells and are a component of the electrode used in gas sensors [17]. Cerium can switch between these two states in a redox process and also exists in the IV state. This finding led to the hypothesis that cerium oxide nanoparticles increase cellular lifespan by scavenging free radicals produced over the course of a cell's lifetime. Ceria nanoparticle unique valence structure promotes cell lifespan, which is a benefit for its antioxidant qualities. The coexistence of CeO_2 nanoparticles in the Ce^{3+} and Ce^{4+} oxidation states has a significant impact on antioxidant behaviour. The energy of cerium dioxide has a large band gap (3.18 eV). Super capacitors, conductor buffer layers, fuel cell work like batteries, buffing and polishing materials, Sun screen, and optical storage systems are just a few of the products that utilise this essential component of technology. Due to its limited size, no crystal is perfect because it could otherwise stretch indefinitely in all directions. This deviation from the optimal cystallinity causes the diffraction peaks to broaden. The two main results from peak width analysis are the crystallite size and lattice strain. Crystallite size is used to determine the coherently diffracting domain size. The particle size and crystallite size are frequently not the same as a result of the creation of polycrystalline aggregates. Lattice strain is used to quantify the distribution of lattice constants brought on by crystal imperfections such lattice dislocations. Other sources of strain include the triple junction at the grain boundary, contact or sinter stresses, stacking faults, and coherency stresses. Crystallite size and lattice strain have varied effects on the Bragg's peak. These two effects suitably alter the position of the two peaks by enlarging and enhancing the peak. The effect of strain, both uniform and non-uniform, on X-ray reflection direction is shown in Figure 1. The transverse reflecting planes shown in Panel (a) on the left represent a portion of an unstrained grain and have a constant equilibrium separation d. On the right, you can see the diffraction line caused by these planes. The corresponding diffraction line shifts to lower angles but otherwise remains unchanged if a uniform tensile strain is given to a grain at right angles to the reflecting planes, as illustrated in panel (b). The X-ray approach used to quantify macrostress is based on this line shift. The grain is bent and the strain is not

uniform in (c): on the top (tension) side, the plane spacing exceeds d, while on the bottom (compression) side, it is less than d, and in the middle, it equals do.

The peak width caused by crystallite size varies as 1/cosθ when strain changes as tanθ. The change in behaviour as a function of 2θ allows for the separation of the size and strain contributions on peak broadening. The Bragg width contribution and crystallite size are inversely correlated. In W-H analysis, a streamlined integral breadth method, size- and strain-induced broadening is deconvoluted by looking at the peak width as a function of 2θ. When compared to TEM imaging, X-ray profile analysis maintains a good position in estimating grain size despite being an averaging method.

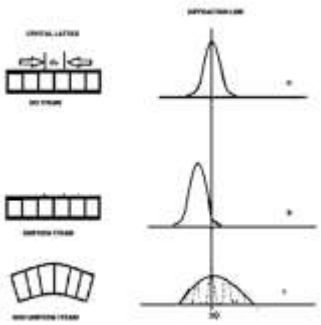

Fig 1 shows portion of an unstrained grain appears in (a) uniform tensile strain (b) Non uniform strain (C) The uniform strain affect the peak position and the non uniform strain affect the peak broadening and intensity.

Experimental:

Using green synthesis method ceria nanoparticle powder was prepared by cerium (III) nitrate hexahydrate powder. A beaker made entirely of pure glass was filled with 5 g of cerium (III) nitrate hexahydrate and 25 ml of distilled water. The mixture was agitated at 60 °C for an hour to create a translucent solution. 10 grams of Artemisia pallens were combined with 50 ml of distilled water, and the combination was cooked at 60 ^{o}C for an hour. After an hour, the solution was filtered, and the filtrates were gathered in a burette. Finally, 50 ml of distilled water was used to dissolve 2 NaOH tablets, which were then dropped into a beaker at a time. Cerium (III) nitrate hexahydrate solution was gradually added drop by drop of this clear solution from the burette. Using a, an alkaline condition was attained. After few hours precipitation formed. After the precipitation the powder dried and then heated with 100 ^{0}C in hot air oven after the heat treatment cerium oxide powder produced [18].

Tin oxide preparation:

10 ml of a 0.5 M $SnCl_4$ solution were used in a clean glass beaker for the sol gel procedure. Ammonia was added after the pH of the solution was adjusted to 9 and heated to 70 ^{0}C.Then, 1 g of acrylamide, 0.25 g of N-N bis methylene acrylamide, a cross-linking polymer that provides a cage-like structure for the Nps to embed themselves in, and 5 mg of ammonium persulphate initiator were carefully added to the beaker where the gels were being produced. The gel is finally dried and turned into tin oxide

powder. The generated tin oxide powder was characterized using a number of tests, including the XRD TEM Raman effect and the UV visible spectrophotometer, and the results were presented in our prior publication [19].

Result and Discussion:

XRD analysis:

Fig. 2 displays the CeO_2 nanoparticle X-ray diffraction pattern for the prepared and annealed powder obtained in the range of (400 ^{0}C, 450 ^{0}C, 500 ^{0}C). The CeO_2 no exhibit several diffraction peaks (111) (220) (311) (400) (331) (422) (511) which can be indexed as single phase cubic structure (JCPDS: 431002). It was clear that when the calcinations' temperature rose; the reflection peaks became sharper, signifying a rise in crystalline. [18] When compared to as prepared CeO_2 confirming that the sample was high quality with excellent crystalline and increased particle size value it is reported in our previous paper [18]. XRD can be used to find the peak broadening with crystallite size and lattice strain (ε) due to dislocation density. The breadth of the Bragg peak is due to the combination of both instrument and sample dependent effects.

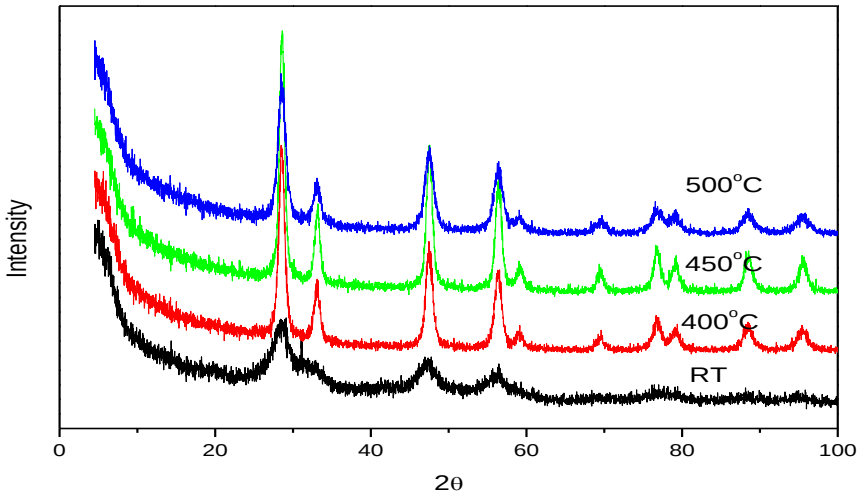

Fig 2 shows XRD diffraction pattern of CeO_2 nanoparticles.

Scherrer Method:

It is used to evaluate peak broadening with crystallite size and lattice strain due to dislocation. The particle size of CeO_2 Nps (varies from 4nm to 16 nm) was determined by the X-ray line broadening method (fig-3) using the scherrer equation.

$$D = \frac{k\lambda}{\beta_{hkl} cos\theta} \quad \text{----------(1)}$$

Where D is the crystallite size and K is the shape factor (0.9) λ is the wavelength of CuKα radiation. The instrument corrected broadening (2θ) β_D corresponding to the diffraction peak of CeO_2 was estimated using the relation

$$\beta_D=[(\beta_D)^2_{\text{measured}} -\beta^2_{\text{Instrument}}]^{1/2} \quad \text{----------(2)}$$

$$\epsilon= \frac{\beta_D}{tan\theta} \quad \text{---------- (3)}$$

Debye Scherrer Method

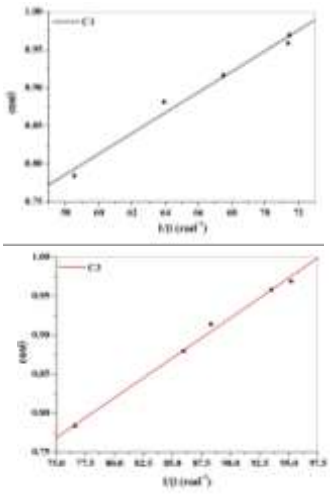

Samples	Grain size (nm)	R^2
C1	10.27	0.9909
C2	12.14	0.9082
C3	13.54	0.9971

Fig 3 shows the crystalline size (D) is extracted from the scherrer plot of CeO_2 nanoparticles at 400 ^{o}C, 450 ^{o}C, 500 ^{o}C.

Monshi Scherrer Method: It is some modification to the earlier scherrer equation in order to compute the crystallite size with higher precision. This method also applied for estimating the crystallite size of CeO_2 nanoparticle

The scherrer equation

$$\beta = \frac{K\lambda}{D} \text{ x } \frac{1}{cos\theta} \text{ ----------(4)}$$

Taking log on both sides

$$In\beta = In\frac{K\lambda}{D} + In\frac{1}{cos\theta} \text{ -------(5)}$$

Fig 4 shown Monshi curve In(β) in y axis v_s $In\frac{1}{cos\theta}$ in x axis has been plotted. Linear fitting of this plot can be compared with straight line equation (y= mx +c) which resulted in the following equation

$$In\frac{1}{cos\theta} = \text{Intercept}$$

Or

$$\frac{K\lambda}{D} = e^{\text{Intercept}}$$

Monshi Method

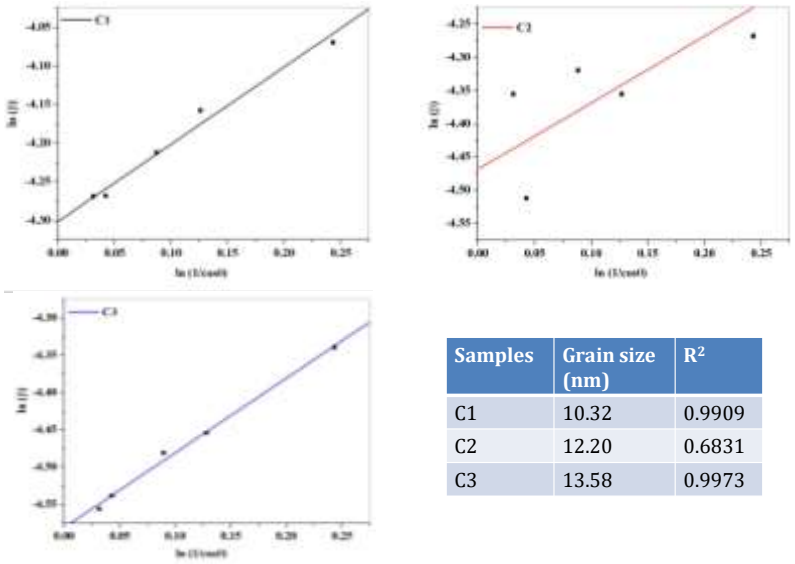

Samples	Grain size (nm)	R^2
C1	10.32	0.9909
C2	12.20	0.6831
C3	13.58	0.9973

Fig 4 shows the crystalline size D is extracted from Monshi plot of CeO_2 nanoparticles at 400 ° C, 450 ° C, 500 °C.

To draw the slope from graph 4 to find the intercept value which is equal to $\ln \frac{K\lambda}{D}$ this value given in the diagram 4.

Williamson Hall method:

Crystallite size of CeO_2 nanoparticle can be compared by another method is called Williamson Hall method. (WHM) . The WHM approach takes into account the effect of strain-induced XRD peak widening in addition to the effect of crystallite size in XRD peak broadening. This W-H model also offers a means to calculate crystallite size and inherent stain. In the W-H model, the change with tanθ in the strain considerations eliminated the 1/cosθ dependency. The imperfections and distortions of a powdered sample's crystals are what produce strain. Strain is caused by crystal flaws and/or distortions, and it can be calculated using the following equation:

$\varepsilon = \beta_{strain}/4\tan\theta$ ----------(6)

Williamson and Hall suggested using the peak width as a function of the diffraction angle 2θ to resolve size and strain broadening.

$$\beta_{hkl} = \frac{k\lambda}{D\cos\theta} + (4 \in \tan\theta) \quad \text{----------(7)}$$

Rearranging

$$\beta_{hkl}\cos\theta = \frac{k\lambda}{D} + (4\in \sin\theta) \text{----------(8)}$$

Williamson - Hall Method

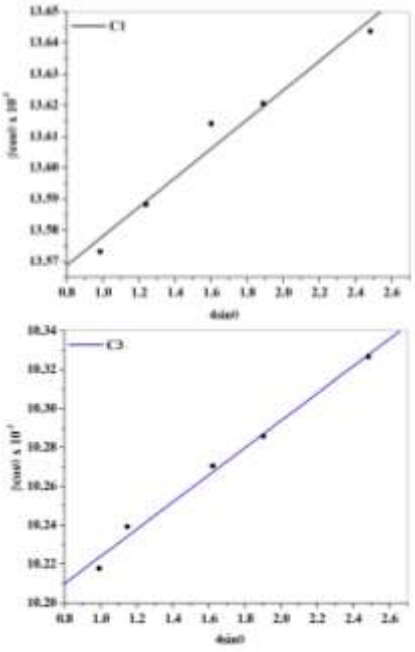

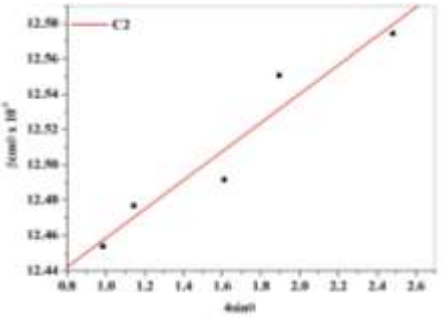

Samples	Grain size (nm)	ε × 10^{-3}	R^2
C1	10.33	5.67	0.9841
C2	12.24	5.78	0.9631
C3	13.55	6.28	0.9953

Fig-5.The W-H analysis of CeO_2 nanoparticle calcined at 400 ^oC, 450 ^oC to 500 ^oC assuming UDM. Fit to the data the strain is extracted from the slope and the crystalline size is extracted from the y intercept of the fit.

Figure 5 was created by plotting 4 sin θ in the x-axis and FWHM total cos in the y-axis. The slope and intercept of the fitted line appear to correlate to the strain and crystal size according to the general WH approach, which generally pertains to an isotropic (perfect) crystal structure. The intercept and slope values from the linear fitting of Fig. 5 were negative and respectively. The crystallite size is calculated to be 10-13 nm.

Fig 5 shows a plot of 4sinθ along x-axis for as prepared and annealed CeO_2 np. From the linear fit to the data the crystallite size was β_{hkl} cosθ along Y-axis for as prepared and annealed CeO_2 np. From the linear fit to the data the crystallite size D was calculated from the Y intercept and the strain ε from the slope of the fit equation 8 represent the uniform deformation method(UDM).Here the strain was uniform in all crystallography directions crystal are isotropic nature. In Fig 5 it is clear that the strain associated with as prepared and annealed samples with as prepared and annealed samples are more or less similar and small indicating that the annealing of CeO_2 sample does not produce any significant effect on strain. Here the stress is proportional to the strain with the constant of proportionality being the Young's modulus denoted by E is given by $\sigma = E\epsilon$ with further increase in strain the particles deviate from the linear proportionality equation 8 may be written as

$$\beta_{hkl}cos\theta = \frac{k\lambda}{D} + \frac{4\,sin\theta_{\sigma}}{E_{hkl}} \quad ---------- (9)$$

Equation 9 represents uniform stress deformation model (USDM). The uniform stress can be calculated from the slope line plotted between 4sinθ /E $_{hkl}$ and $\beta_{hkl}cos\theta$ (fig-4) and the crystallite size D from the intercept.

The strain ϵ can be measure if E $_{hkl}$ of cubic CeO_2 np are known. In equation 9 the assumption of homogeneity and isotropy is not justified. Moreover the constants of proportionality associated with the stress-strain relation are no longer independent when the strain energy density U is considered [20-21]. According to Hooke's law the energy density as a function of strain is

$$U=(\epsilon^2 E_{hkl})/2 \quad \text{---------(10)}$$

Equation 7 modified as

$$\beta_{hkl}cos\theta = \frac{k\lambda}{D} + (4\ \sin\theta\ (2U/E_{hkl})^{1/2}) \quad \text{--------(11)}$$

Uniform deformation energy density model:

Plot (fig-4) of $\beta_{hkl}cos\theta$ vs $(4\ \sin\theta\ (2U/E_{hkl})^{1/2})$ was constructed and the data fitted to line. The anisotropic energy density was estimated from the slope of crystallite size from the Y intercept. Equation 11 represents UDEDM, the crystals are assumed to have a homogeneous, isotopic nature. (Fig-5).

EDXA:

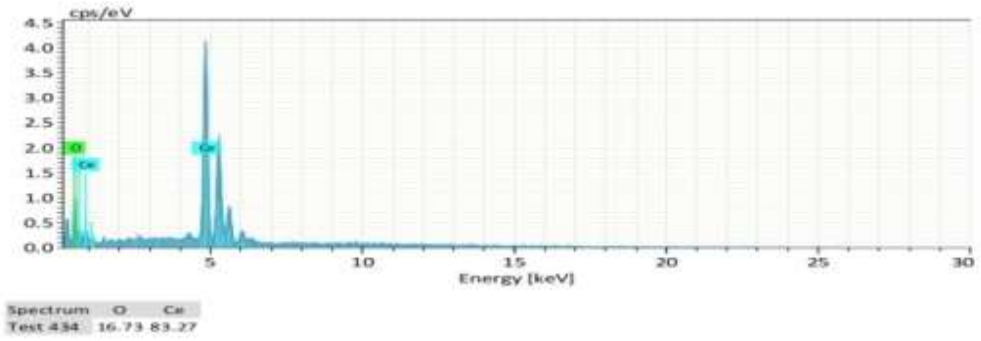

Fig 6 shows EDXA formed at 500 ^{0}C samples

The Quantative elemental composition of the most sensitive nanocrystalline CeO_2 nanoparticles was analysed using energy dispersive spectrometer at 500 ^{0}C as shown in fig-6 From the table 1 it is clear that as prepared CeO_2 nanoparticle was observed to nonstoichiometric in nature[18].

Quantative elemental analysis as prepared CeO2 nanoparticles for 500 ^{0}C samples

Element	Observed		Without heating	
	Mass %	at %	Mass %	at %
O	16.73	36.24	31.02	79.81
Ce	83.27	63.76	68.91	20.19
Total	100	100	100	100

SEM/TEM:-

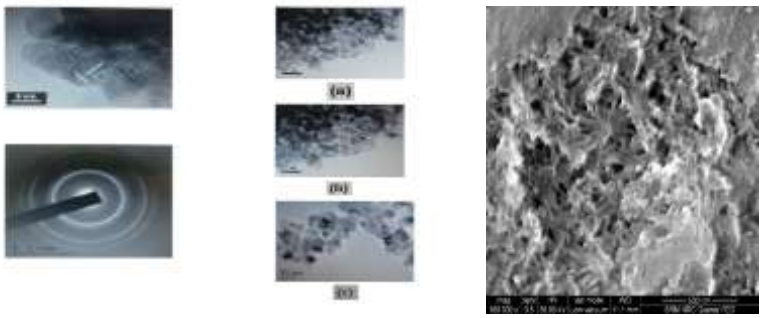

Fig 7 shows TEM-SEM images of CeO2 nanaparticles after calcinations temperature 400-500 ^{0}C samples

TEM is the best method for analyzing the shape and size of nanoparticles. Figure 7 displays the TEM image of cerium oxide nanoparticles. It was discovered that the TEM image showed particles with a size between 4 and 16 nm. The selected region diffraction pattern of the cerium oxide nanoparticles calcined at 450 ^{0}C indicates the multilayered pattern of the particle revealed in the HRTEM data. It was discovered that the cerium oxide nanoparticles had a smooth surface and a spherical form. The typical separation between two consecutive fringes in the HRTEM pattern is 0.31 nm.

UV/Visible Reflectance spectra:

The diffuse reflectance spectra of CeO_2 Nps are displayed in Fig. 8. This discovery is used to identify direct semiconductors with a bandgap (3.45eV). Bulk CeO_2 has an optical bandgap of 3.22 eV. the quantum size effect's improvement of CeO2 Nps' optical band gap. Its foundation is the surface dispersion of a portion of the incident UV visible light. According to the observational findings, a combination of optical processes causes the sample surface to reflect radiation onto the entire overlaying hemisphere.

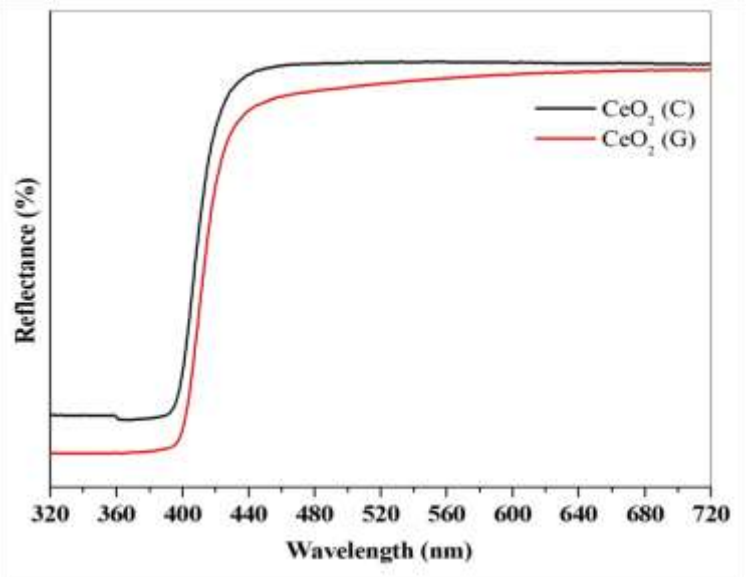

Fig-8 shows the UV-Visible Diffuse Reflectance Spectra of CeO_2 NPs

Fourier Transform Infrared Spectroscopy studies

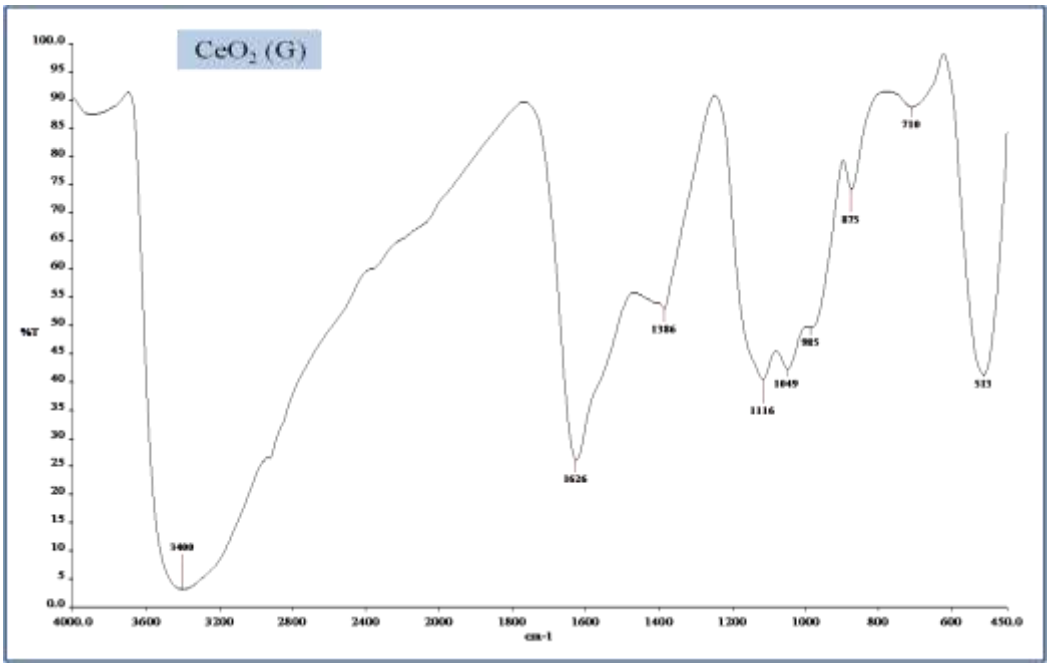

Fig-9 shows the FTIR Spectra of CeO_2 NPs

In order to identify the vibrational modes and chemical composition of CeO_2 NPs FTIR spectra have been recorded in 500–4000 cm^{-1} wavelength range, as shown in Figure 9. The absorption bands at *3395 and *835 cm^{-1} are due to Ce-OH and Ce-O stretching modes, respectively. Whereas the bands at *1577 and *1383 cm^{-1} are related to OH and C=O bending vibrations. Furthermore, the band at *1066 cm^{-1} corresponds to C-OH functional groups and the band at *2000–2350 cm^{-1} can be attributed to the carbonyl group and atmospheric CO_2 absorption on cationic ions. It can be noted that the broadening and shifting in these modes confirm the successful formation of pristine CeO_2.

Photocatalyst:

The dyes are used in textile industries and paper industries; they are utilising a lot of methylene blue (MB) dye. Because MB is extremely toxic, carcinogenic, and non-biodegradable, its presence in wastewater poses a serious hazard to both environmental and human health. Ingestion of MB in human body through contaminated drinking water or food, can cause irritation of skin, mouth, and stomach; nausea, headache, vomiting, anemia & diarrhea. Therefore, the pre-treatment of wastewater contaminated with MB dye becomes necessary for maintaining the quality of water and its safer use.

Photocatalytic degradation study:

In the presence of cerium oxide nanoparticles, tin oxide Nps the photodegradation of MB was investigated. Methylene blue (MB) was subjected to photocatalytic degradation in its aqueous solution under UV light while being conducted at room temperature. In a pyrex reactor tube, a defined quantity of the photocatalyst powder was typically completely mixed with the MB dye solution at the specified concentration. It was then exposed to a UV lamp (Philips) that emitted radiation primarily at 365 nm. The UV lamp was placed parallel to the reactor tube at a distance of 6 cm, with a defined power of 12 W, 230 Volts, and 50 Hz. Drop wise additions of 0.1M NaOH or 0.1M HCl solution were used to adjust the reaction mixture's pH, and the external mass transfer effect was removed by stirring the mixture at 3000 rpm. The reaction mixture was magnetically agitated in the dark for 15 minutes prior to UV radiation in order to create the adsorption/desorption equilibrium of methylene blue. Every 10 minutes, 5 ml of the reaction mixture were taken out and centrifuged at 4000 rpm for 20 minutes. The methylene blue content in the supernatant liquid was then calculated spectrophotometrically by recording absorbance at 665 nm. Using equation 12, the % deterioration of MB was determined.

$$\text{Degradation (\%)} = (C_0 - C_t)/C_0 \times 100 \quad \text{----------(12)}$$

For an initial MB concentration of 5, 15, 25, and 40 mg/l at PH 11, the apparent rate constant of the degrading reaction catalysed by 1.0 g/L of nanosized CeO_2 was computed.

$$\text{In } C_0/C_t = K_{app}.t$$

Where C is the concentration of the dye (mg/L) t is the irradiation time (min) and Kapp is the apparent rate constant. (min^{-1})

Degradation of the MB molecules occurred under UV-visible irradiation in the presence of Cerium oxide nanoparticles leads to an increase in degradation efficiency. As a semiconducting material, cerium oxide will begin to absorb light at wavelengths less than 420 nm [20]. As a result, radiation with a wavelength of less than 420 nm is ideal for transferring electrons from the VB to CB. As a result, the valence and conduction bands, respectively, create electrons and holes. Hydroxyl species are produced when the positive holes react with the water that has been absorbed. The nonosized cerium oxide produced after calcinations at 500 ^{0}C shows the highest photocatalytic activity among the prepared nanopartciles photocatalytic activity is affected by particle size crystallinity and surface properties. These factors are controlled by changes in the preparation method, the co catalysts loading and foreign elements.

Photocatalyst load dependent kinetic of methylene blue (MB) degradation behaviour was examined in the light of pseudo first order kinetic model that can be represented by equation 13

$\ln(C_0/C_t) = k.t$ ----------(13)

Where, Co and Ct represent MB concentrations at initial stage (zero time) and at time t, respectively. Plots of ln(C0 /Ct) versus time (t) for degradation of MB in its 10 mgL-1 aqueous solution at varying cerium oxide load are shown in Fig-10. The observed linearity in these plots proves the applicability of the pseudo first order kinetic model for the photocatalytic degradation of MB in aqueous medium over the studied. The rate constant (k) for MB degradation at any catalyst (CeO_2) load, was obtained from the slope of the corresponding plot as shown in table-2.

Table-2 shows Photo degradation of cerium oxide nanoparticles formed at 450 ^{0}C

Material	**Dye concentration (mg/L)**	**K app/min$_{10^{-3}}$**	**1/Kapp**	**$t_{1/2}$ / min**	**Regression coefficient R**
ceriumoxide	5	14.93	6.697	46.42	0.965
	10	9.30	105.18	74.22	
	15	8.70	114.6	79.51	
	25	4.57	217.1	150.9	
	40	4.02	249.8	172.9	

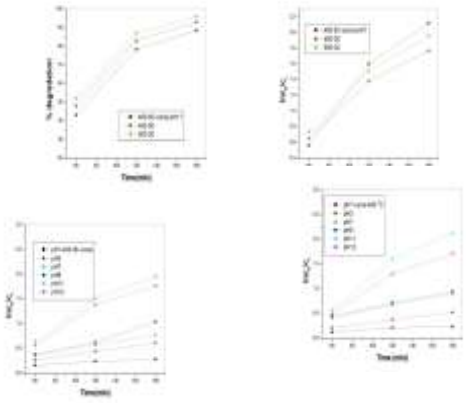

Fig-10 shows % degradation of MB dye by CeO2 nanoparticles at different pH, degradation of MB dye and kinetic curve by CeO2 at various temperature.

Effect of PH:-

The ideal pH of the reaction medium must be chosen in order to achieve the greatest possible breakdown of organic pollutants like MB. This is due to the fact that pH influences the kind and strength of net electrical charge on the catalyst surface as well as the net charge on the molecules of the substrate (MB). According to the degree of ion-ion attraction or repulsion, both of these variables influence the amount of dye molecule adsorption at the photocatalyst (CeO2), which in turn influences the rate of photocatalytic molecular breakdown of the substrate (MB). Figure 10 displays plots of the percentage of MB photocatalytic degradation as a function of reaction time at different aqueous medium pH and temperature. Photocatalytic degradation of MB efficiency occurs when the pH of the solution is raised from 1 to 12. MB was degraded by 96% when exposed to UV light. ideal pH of 11 and catalyst load of 5 mgL-1. The increased hydroxyl ions in the aqueous medium, which react with the photogenerated holes (h+) to produce more hydroxyl radicals (OH) required for photocatalytic degradation of MB, may be the cause of the observed increasing MB degradation at higher pH (until the optimal pH). Variations in the photocatalyst's surface charge characteristics can also be used to explain the rise in MB degradation at higher pH values. MB adsorption at the catalyst surface is a pre-requirement for photocatalytic reaction; the dye degradation would obviously be faster at higher pH. However, the decrease in MB degradation at still higher (pH=11) could be due to alkaline dissolution of $Ce0_2$ pH dependent degradation kinetic.[22-25]

Effect of methylene blue concentration:

Experiments were conducted using beginning concentrations of substrate (MB) ranging from 5 to 40 mgL-1 in order to investigate the impact of MB initial concentration on its breakdown. Using different starting MB concentrations, Fig. 11 displays the plots of MB percent degradation as a function of time (min) (optimal catalyst load: 5 mgL-1; pH: 11). It was discovered that when the initial concentration of MB increased, the percentage of degradation decreased.

It might be because, for the specified catalyst load, the number of surface active sites per dye molecule reduces as MB concentration rises. In addition, at larger dye concentrations, the intensity of photons reaching the catalyst surface decreases because some UV radiation is absorbed by dye molecules in solution, which lowers the pace at which methylene blue degrades.

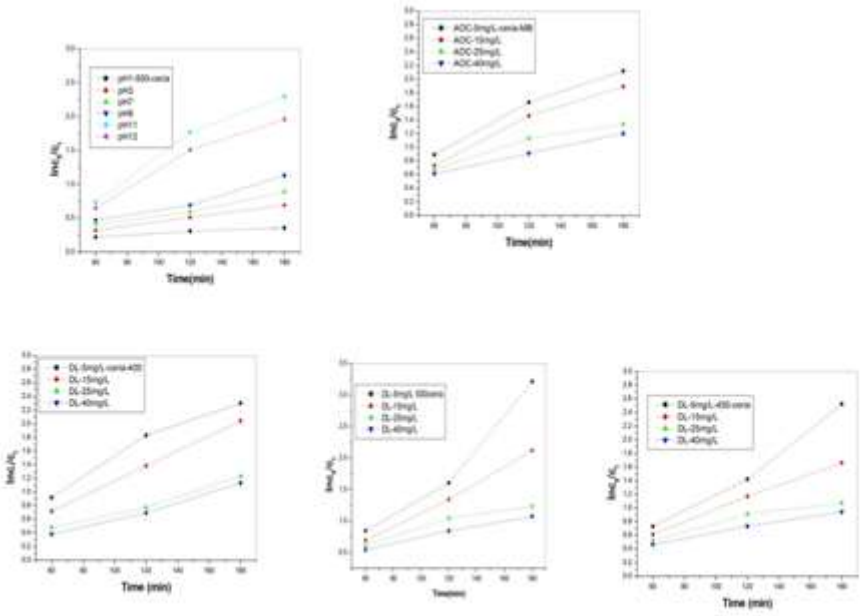

Fig-11 shows Degradation efficiency of MB (CeO2) and kinetic curve various dye loading and degradation efficiency and kinetic curve various amount of catalysts.

Tin oxide:

Similarly the photocatalytic degradation of MB in aqueous medium were carried out by four different temperature such as 300 ^{0}C , 400 ^{0}C, 500 ^{0}C,600 ^{0}C was studied. The optimal degradation was achieved at 300 °C, with a corresponding catalyst concentration of 30 mg/L and dye loading of 20 mg/L. Figure 12 displays plots of the percentage of MB photocatalytic degradation as a function of reaction time at different aqueous medium pH values. Photocatalytic decrease of MB efficiency occurs when the pH of the solution is raised from 3 to 12. MB was degraded by 86% when exposed to UV light. The slope of the corresponding plot was used to determine the rate constant (k) for MB degradation (table-3) at any catalyst (SnO2) load. [19]

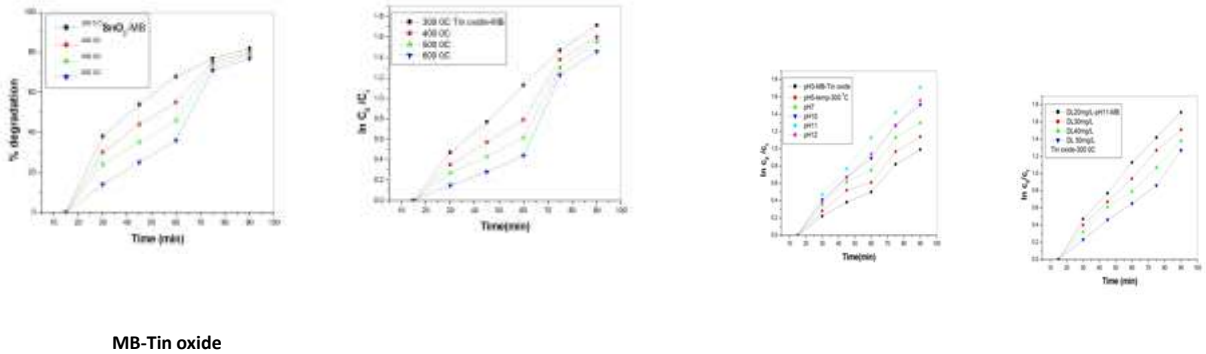

MB-Tin oxide

Plots of percentage of degradation /Inc0/ct as a function of time (min) at varying temperatures

Fig-12 shows Degradation efficiency of MB dye (SnO_2) and kinetic curve various dye loading and degradation efficiency and kinetic curve various amount of catalysts.

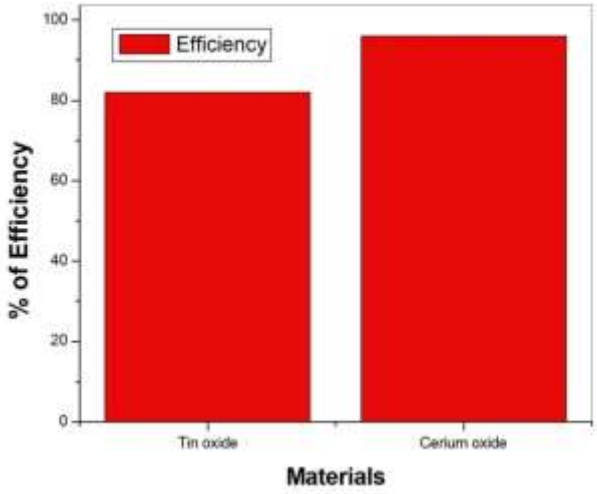

Fig-13 shows the removal of various dye photocatalysis process by cerium oxide and tin oxide catalysis.

BET surface:

According to Brunauer Stephen-Emmett Paul Hugh-Teller Edward (BET) hypothesis, gas molecules can physically adsorb or physisorb onto solid surfaces. Kinetic adsorption and the rate of adsorption or desorption are explained by BET, an extension of the Langmuir model that also applies to monolayer molecule adsorption. The surface area analysis is computed using the following assumptions.

1. Gas molecules can physically adsorb indefinitely in layers on a solid.
2. Only nearby layers are impacted by gas molecules.
3. Every layer can benefit from the application of Langumuir theory.

4. The first layer's enthalpy of adsorption is constant and higher than the second's.
5. The second layer's enthalpy of adsorption and liquefaction are identical.

Using the same technique as for handling experimental data, BET surface areas were derived from the computed isotherms. It is a crucial analytical method for determining a material's specific surface area. The BET theory is applicable to multilayer adsorption systems that typically use nitrogen or probing gas adsorption. This theory directly measure surface area and pore size distribution.

AUTOSORB-1 (Quantachrome Instruments) nitrogen adsorption apparatus was used for the determination of the Brunauer–Emmett–Teller (BET) surface area (*S*BET) of the Ceria powders calcined at different temperatures. Before measuring nitrogen adsorption, the calcined samples were degassed at 453 K and the as-prepared sample was degassed at 353 K. The BET surface area was calculated using the multipoint BET method and the adsorption data in the relative pressure (P/P0) range of 0.05–0.3. The desorption isotherm was used to calculate the pore size distribution using the cylindrical pore size and the Barret–Joyner–Halender (BJH) technique [26]. As indicated in table 4, the nitrogen adsorption volume at the relative pressure (P/P0) of 0.994 was used to calculate the pore volume and average pore size.

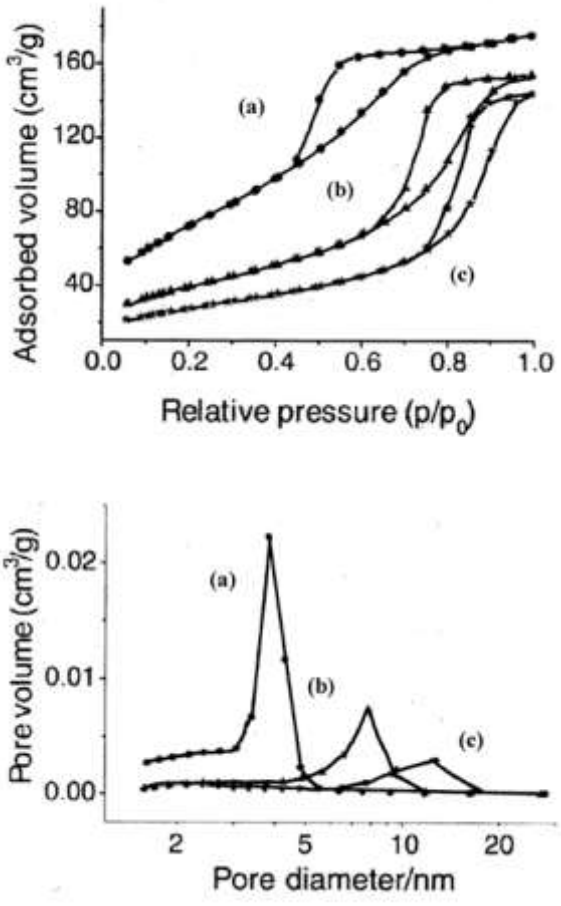

Fig.14 shows - Mesoporous CeO_2 nanoparticles' N_2 adsorption-desorption isotherms and pore size distribution. Temperature-dependent synthesis (a) without HT (b) 400 ^{0}C (c) 450 ^{0}C

Fig. 14 shows the nitrogen adsorption–desorption isotherms of the samples calcined at different temperature. The as prepared and calcined samples exhibited the isotherms of type IV (BDDT classification) [27]. Hysteresis loops of type H_3 at high relative pressures from 0.4 to 1.0. The hysteresis loops shifted to the region of higher relative pressure and the areas of the hysteresis loops gradually became small with increase of calcinations temperature. The pore size distribution curve of the samples that were calcined at different temperatures is shown in a separate figure below. It is evident from the figure that the pores' diameter ranged from 2.0 to 16.0 nm, with an average diameter of no more than 10 nm (as indicated in Table). CeO2 particle aggregation is responsible for the samples' development of mesoporous structure [27]. The average pore size rose from 3.3 to 9.1 nm as the calcination temperature rose. Smaller pores were able to collapse during calcinations because they were subjected to more stress than bigger holes. Additionally, larger pores might develop into even larger pores. Therefore, pore size grew while pore volume decreased as the calcination temperature rose.

.

Conclusion:

This paper reports on the photocatalytic performance of cerium oxide and tin oxide Nps catalyzed by MB dye degradation. Both compounds are made using the acrylamide technique and green synthesis. While a lot of chemicals were needed to make the tin oxide powder in the acrylamide approach, only a few chemicals were needed to make cerium oxide in this green synthesis method. The green synthesis approach yields the best photocatalyst for environmental solutions and very small particle size. Cerium preparation involved using cerium (iii) nitrate hexahydrate solution as the starting material for the co-precipitation method, which uses a green synthesis process to create CeO2 nanoparticles. The capping and reducing agent was an extract from the leaves of Artemisia pallens. The CeO2 nanoparticle was characterized by X-ray diffraction, and the WH analysis was utilized to determine the particle size, lattice strain, stress, and energy density from the XRD data. CeO2 samples' surface characteristics were examined using TEM and SEM. Once again, the oxygen and Ce elements present in the processed samples match the EDXA spectra. The cerium oxide material showed good photocatalytic performance. The findings showed that the best photocatalyst for the degradation of MB is ceria Nps, which is smaller than tin oxide. The photogenerated holes are the main CeO2 active species in the photocatalytic breakdown of MB. The results showed that smaller CeO2 nanoparticles could act as photocatalysts for the breakdown of MB. When CeO_2 is calcined at 500^0C, the MB degradation exhibits the maximum photo catalytic reactivity at pH 11. The colour of MB is noticeably reduced when superoxide radicals and OH are present. CeO_2's surface area and crystal structure both affect how well the catalyst removes MB dye. As the catalyst's surface area grows, so does the removal through the adsorption mechanism. It was found that pores had an average width of less than 10 nm and varied in size from 2 to 16 nm using BET surface theory. As the calcination temperature increased, the average pore size increased from 3.3 to 9.1 nm.

Reference:

1. Korsvik, C., S. Patil, et al. (2007). "Superoxide dismutase mimetic properties exhibited by vacancy engineered ceria nanoparticles." Chemical Communications(10): 1056. https://doi.org/10.1039/B615134E

2. Zhou, J., L. Zhao, et al. (2008). "Catalytic Activity of Y Zeolite Supported CeO2 Catalysts for Deep Oxidation of 1, 2-Dichloroethane (DCE)." Catalysis Letters **127**(3): 277. https://doi.org/10.1007/s10562-008-9672-5

3. Zheng, X., X. Zhang, et al. (2007). "Effect of Addition of Base on Ceria and Reactivity of CuO/CeO2 Catalysts for Low-Temperature CO Oxidation." Journal of Natural Gas Chemistry **16**(2): 179-185. https://doi.org/10.1016/S1003-9953(07)60045-0

4. Zhu, B., X. Liu, et al. (2003). "Calcium doped ceria-based materials for cost-effective intermediate temperature solid oxide fuel cells." Solid State Sciences **5**(8): 1127-1134. https://doi.org/10.1016/S1293-2558(03)00123-7

5. Zhang, T. S., J. Ma, et al. (2004). "Aging behavior and ionic conductivity of ceria-based ceramics: a comparative study." Solid State Ionics **170**(3): 209-217. https://doi.org/10.1016/j.ssi.2004.03.003

6. Zhu, B., X. Liu, et al. (2003). "Calcium doped ceria-based materials for cost-effective intermediate temperature solid oxide fuel cells." Solid State Sciences **5**(8): 1127-1134. https://doi.org/10.1016/S1293-2558(03)00123-7

7. Hibino, T., K. Ushiki, et al. (1997). "Electrochemical oxygen pump using CeO2-based solid electrolyte for NOx detection independent of O2 concentration." Solid State Ionics **93**(3): 309-314. https://doi.org/10.1016/S0167-2738(96)00541-3

8. Lima, J. F. d., R. F. Martins, et al. (2009). "ZnO:CeO2-based nanopowders with low catalytic activity as UV absorbers." Applied Surface Science **255**(22): 9006-9009. https://doi.org/10.1016/j.apsusc.2009.06.071

9. Zhang, Y., M. Hida, et al. (2000). "Effect of rare-earth oxide (CeO2) on the microstructures in laser melted layer." Journal of materials science **35**(21): 5389-5400. https://doi.org/10.1023/A:1004807214957

10. Sinha, A. K. and K. Suzuki (2005). "Preparation and Characterization of Novel Mesoporous Ceria−Titania." The Journal of Physical Chemistry B **109**(5): 1708-1714. https://doi.org/10.1021/jp046391b

11. Jiang, K., J. Meng, et al. (1999). "Sol-gel synthesis and electrical properties of ceria-based solid electrolytes." Science in China Series B: Chemistry **42**(2): 159-163. https://doi.org/10.1007/BF02875512

12. Courbiere B, Auffan M, Rollais R, Tassistro V, Bonnefoy A, Botta A, Rose J, Orsière T, Perrin J. Ultrastructural interactions and genotoxicity assay of cerium dioxide nanoparticles on mouse oocytes. Int J Mol Sci. 2013 Oct 31;14(11):21613-28. https://doi.org/10.3390/ijms141121613

13. De Marzi, L., A. Monaco, et al. (2013). "Cytotoxicity and genotoxicity of ceria nanoparticles on different cell lines in vitro." International journal of molecular sciences **14**(2): 3065-3077. https://doi.org/10.3390/ijms14023065

14. Demokritou P, Gass S, Pyrgiotakis G, Cohen JM, Goldsmith W, McKinney W, Frazer D, Ma J, Schwegler-Berry D, Brain J, Castranova V. An in vivo and in vitro toxicological characterisation of realistic

nanoscale CeO_2 inhalation exposures. Nanotoxicology.2013Dec;7(8):1338-50. https://doi.org/10.3109/17435390.2012.739665

15. Peng L, He X, Zhang P, Zhang J, Li Y, Zhang J, Ma Y, Ding Y, Wu Z, Chai Z, Zhang Z. Comparative pulmonary toxicity of two ceria nanoparticles with the same primary size. Int J Mol Sci. 2014 Apr 10;15(4):6072-85. https://doi.org/10.3390/ijms15046072

16. Pulido-Reyes, G., I. Rodea-Palomares, et al. (2015). "Untangling the biological effects of cerium oxide nanoparticles: the role of surface valence states." Scientific Reports **5**(1): 15613. https://doi.org/10.1038/srep15613

17. Dahle JT, Arai Y. Environmental geochemistry of cerium: applications and toxicology of cerium oxide nanoparticles. Int J Environ Res Public Health. 2015 Jan 23;12(2):1253-78. https://doi.org/10.3390/ijerph120201253

18. Ramanathan, G., S. V. Rathan, et al. (2018). "Photocatalytic activity of biosynthesized CeO2 nano particles." SN Applied Sciences **1**(1): 116. https://doi.org/10.1007/s42452-018-0103-y

19. Ramanathan.G Murali K R (2022) "Photocatalytic activity of SnO2 nanoparticles" Journal of Applied Electrochemistry 52 849-859 https://doi.org/10.1007/s10800-022-01676-z

20. Yogamalar, R., R. Srinivasan, et al. (2009). "X-ray peak broadening analysis in ZnO nanoparticles." Solid State Communications **149**(43-44): 1919-1923. https://doi.org/10.1016/j.ssc.2009.07.043

21. Zak, A. K., W. A. Majid, et al. (2011). "X-ray analysis of ZnO nanoparticles by Williamson–Hall and size–strain plot methods." Solid State Sciences **13**(1): 251-256. https://doi.org/10.1016/j.solidstatesciences.2010.11.024

22. Pouretedal, H. and A. Kadkhodaie (2010). "Synthetic CeO2 nanoparticle catalysis of methylene blue photodegradation: kinetics and mechanism." Chinese Journal of Catalysis **31**(11-12): 1328-1334. https://doi.org/10.1016/S1872-2067(10)60121-0

23. Yin, J., S. Huang, et al. (2015). "Fabrication of heterojunction SnO2/BiVO4 composites having enhanced visible light photocatalystic activity." Materials Science in Semiconductor Processing **34**: 198-204. https://doi.org/10.1016/j.mssp.2015.02.044

24. Srinivasan, N., M. Anbuchezhiyan, et al. (2019). "Hydrothermal synthesis of C doped ZnO nanoparticles coupled with BiVO4 and their photocatalytic performance under the visible light irradiation." Applied Surface Science **494**: 771-782. https://doi.org/10.1016/j.apsusc.2019.07.093

25. Ramanathan.G, Murali K.R "Photocatalytic activity of SnO2 nanoparticles" Journal of Applied Electrochemistry 52 849-859 (2022) https://doi.org/10.1007/s10800-022-01676-z

26. Gnanasekaran, L., R. Hemamalini, et al. (2017). "Synthesis and characterization of metal oxides (CeO2, CuO, NiO, Mn3O4, SnO2 and ZnO) nanoparticles as photo catalysts for degradation of textile dyes." Journal of Photochemistry and Photobiology B: biology **173**: 43-49. https://doi.org/10.1016/j.jphotobiol.2017.05.027

27. K. S. W. Sing, D. H. Everett, R. A. W. Haul, L. Moscou, R. A. Pierotti, J. Rouquerol and T. Siemieniewska, "Reporting Physisorption Data for Gas/Solid Systems with Special Reference to the

Determination of Surface Area and Porosity," Pure and Applied Chemistry, Vol. 57, No. 4, 1985, pp. 603-619. doi/10.1351/pac198557040603

27.Yu, J., J. C. Yu, et al. (2003). "Effects of acidic and basic hydrolysis catalysts on the photocatalytic activity and microstructures of bimodal mesoporous titania." Journal of Catalysis **217**(1): 69-78. https://doi.org/10.1016/S0021-9517(03)00034-4